

# Volatile Organic Compound Detection Using Insect Odorant-Receptor Functionalised Field-Effect Transistors

by

Eddyn Oswald Perkins Treacher

A thesis submitted in fulfilment of the  
requirements of the degree of  
Doctor of Philosophy in Physics  
School of Physical and Chemical Sciences  
Te Herenga Waka - Victoria University of Wellington

Apr 2024





# Table of contents

|  |           |
|--|-----------|
| <b>Acknowledgements</b>  | <b>1</b>  |
| <b>1. Biosensing with Insect Odorant-Receptor Functionalised Carbon Nanotube Devices</b>               | <b>3</b>  |
| 1.1. Introduction . . . . .  | 3         |
| 1.2. Aqueous Sensing of Ethyl Hexanoate with OR22a-functionalised Carbon Nanotube Transistor . . . . . | 3         |
| 1.2.1. OR Nanodisc Functionalisation . . . . .   | 3         |
| 1.2.2. Aqueous Sensing of Ethyl Hexanoate . . . . .  | 8         |
| 1.3. Addressing Biosensor Variability . . . . .  | 12        |
| 1.3.1. Variability in Biosensor Behaviour . . . . .  | 12        |
| 1.3.2. Potential Sources of Variability . . . . .  | 18        |
| 1.4. Vapour Sensing . . . . .  | 24        |
| 1.5. Conclusion . . . . .  | 24        |
| <b>Appendices</b>  | <b>25</b> |
| <b>A. Vapour System Hardware</b>   | <b>25</b> |
| <b>B. Python Code for Data Analysis</b>  | <b>27</b> |
| B.1. Code Repository . . . . .   | 27        |
| B.2. Atomic Force Microscope Histogram Analysis . . . . .  | 27        |
| B.3. Raman Spectroscopy Analysis . . . . .   | 27        |
| B.4. Field-Effect Transistor Analysis . . . . .  | 27        |



# Acknowledgements

69450

Rifat, Alex - vapour sensor  
Erica Cassie - FET sensing setup  
Rob Keyzers and Jennie Ramirez-Garcia - NMR spectra  
Patricia Hunt - Computational chemistry



# **1. Biosensing with Insect Odorant-Receptor Functionalised Carbon Nanotube Devices**

## **1.1. Introduction**

To test devices with the new vapour delivery system, it was important to first ensure the functionalised devices worked consistently as biosensors in the existing aqueous sensing setup.

## **1.2. Aqueous Sensing of Ethyl Hexanoate with OR22a-functionalised Carbon Nanotube Transistor**

### **1.2.1. OR Nanodisc Functionalisation**

A carbon nanotube network field-effect transistor device, fabricated using post-June 2023 methods as described in ?@sec-fabrication, was functionalised with OR22a nanodiscs. The network used for the device was deposited using the steam-assisted surfactant method, and the device was encapsulated with AZ® 1518 using the post-Jan 2023 photolithography mask. The functionalisation was performed as follows:

1. The device was exposed to UV light for 1 minute, placed in AZ® 326 developer for 3 minutes, then rinsed with acetone, isopropanol and nitrogen dried.
2. The device was vacuum annealed for 1 hour at 150°C.

Note: Steps 1 & 2 were added to ensure any residual photoresist on the channel was removed or passivated before functionalisation, see ?@sec-photoresist-contamination.

3. A solution of 1 mM PBASE (Setareh Biotech) in methanol was prepared by fully dissolving 2 mg PBASE in 5 mL methanol by vortex mixing at 1000 rpm in a dark room.

## *1. Biosensing with Insect Odorant-Receptor Functionalised Carbon Nanotube Devices*

Note: PBASE was stored at -18°C for 18 months prior to use, and was thawed under vacuum for 15 minutes in dark conditions before opening.

4. The device was then rinsed with methanol, fully submerged in ~ 1 mL of PBASE in methanol solution and left covered with parafilm for 1 hour, then rinsed with methanol for 15 s, rinsed with 1XPBS for 15 s and nitrogen dried to remove residual PBASE.
5. The device was left dry and in darkness while collecting the OR22a nanodiscs from the -80°C freezer.
6. 10 µL OR22a nanodiscs (batch number ND-OR22a-SB018, 1.9 mg/mL, prepared 7 months earlier) were diluted in 1 mL 1XPBS

Note: The full 1 mL was used to flush out the nanodisc vial when preparing the nanodisc solution, with successive additions and subtractions of 50 µL 1XPBS into and from the vial.

7. The device was submerged in the OR22a nanodisc solution and left covered with parafilm for 1 hour, then rinsed with 1XPBS for 15 s and gently nitrogen dried.

Liquid-gated electrical characteristics were taken of the sensing channel (channel 7) before and after functionalisation with OR22a. These electrical characteristics were taken in using a liquid gate buffer of 1XPBS containing 0.5% DMSO with the B1500A semiconductor device analyser. These characteristics are shown in Figure 1.1, shown using both a logarithmic and linear current scale. The device exhibited ambipolar characteristics before functionalisation, which is typically seen for steam-deposited carbon nanotube films ([?@sec-cnt-devices](#)). However, *p*-type behaviour dominates after device functionalisation due to a significant drop in *n*-type conductance. There was little hysteresis present, which is also typical for these devices. A slight increase in hysteresis was observed post-functionalisation. Leakage current (shown by the dashed traces) never exceeds  $1 \times 10^{-7}$  V, both before and after functionalisation. The significant change in electrical characteristics observed could be due to five possible factors — adsorption of solvent onto the network, network attachment of PBASE without subsequent protein attachment, non-specific adsorption of protein onto the network, PBASE-mediated attachment of the membrane scaffold protein (MSP) of nanodiscs to the network, and PBASE-mediated attachment of odorant receptors to the network. Note that as the nanodisc volume is much larger than that of the odorant receptor, any direct protein adsorption is highly likely to be adsorption of the nanodisc membrane scaffold protein onto the carbon nanotube network. Odorant receptor attachment via PBASE is therefore the only desirable functionalisation result for sensing purposes.

Only minor changes were observed in the on-off ratio when comparing the device channel before and after functionalisation. The on-off ratio for the pristine channel was  $1120 \pm 220$ , fairly typical for a transfer curve from a steam-assisted surfactant-deposited CNT network device (see [?@sec-cnt-devices](#)). The on-off ratio increased slightly to

## 1.2. Aqueous Sensing of Ethyl Hexanoate with OR22a-functionalised Carbon Nanotube Transistor

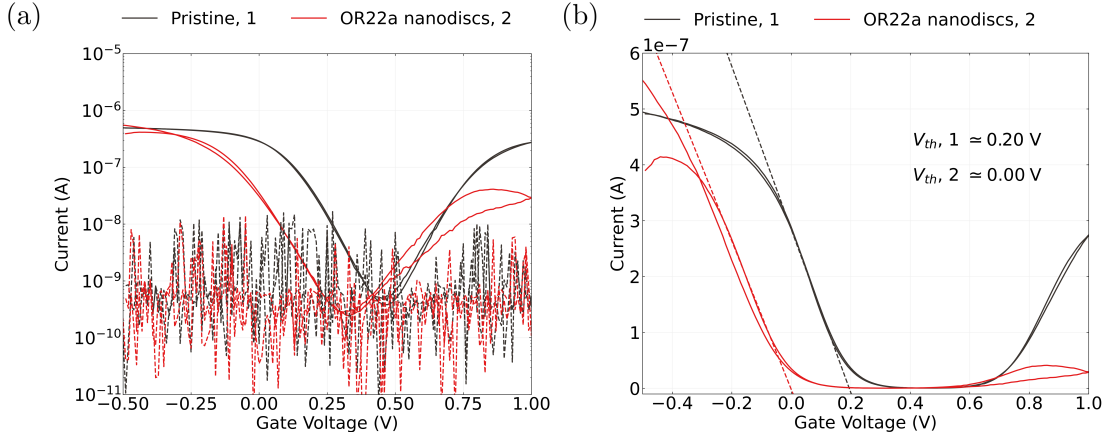


Figure 1.1.: Liquid-gated carbon nanotube network device transfer characteristics before and after OR22a nanodisc functionalisation. In (a), the characteristics are shown on a logarithmic scale, where the gate current for each transfer curve is shown with a dashed line. In (b), the characteristics are shown on a linear scale alongside a dashed line tangent to the subthreshold slope of the characteristic curve. The threshold voltage corresponding to the intercept of this slope with the x-axis is shown for each transfer characteristic curve.

$1830 \pm 550$  after functionalisation. We expect to see an increase in on-off ratio for a device successfully functionalised with OR22a, which may result from an increase in negative charge causing modulation of Schottky barriers between metallic and semiconducting carbon nanotubes within the network [1]. However, we also expect increased hole conductance from the attachment of PBASE, even without proteins being present ([?@sec-PBASE-electrical-characterisation](#)). It is therefore difficult to determine whether functionalisation has been successful from the on-off ratio of transfer characteristics alone.

Functionalisation of the channel resulted in a negative shift in threshold voltage of  $-0.20 \pm 0.03$  V. This is significantly in excess of threshold voltage shifts measured for both methanol adsorption ( $-0.15 \pm 0.02$  V) and after exposure to PBASE in methanol ( $-0.06 \pm 0.04$  V), confirming that protein has attached to the carbon nanotubes. However, both direct protein adsorption [2], [3] and empty nanodisc attachment [1] should also lead to a significant negative threshold voltage shift in the liquid-gated transfer characteristic curve. In all three cases, the voltage shift is predominantly the result of negative charge transfer from the adsorbed proteins to the semiconducting carbon nanotubes [1]–[3]. It is likely that the negative shift observed results from some combination of the three types of attachment. It should be noted that while the size of the functionalisation-induced threshold voltage shift can be used to determine whether protein has attached to the nanodisc network, it cannot be used to specifically determine whether odorant receptors have attached to the network.

## 1. Biosensing with Insect Odorant-Receptor Functionalised Carbon Nanotube Devices

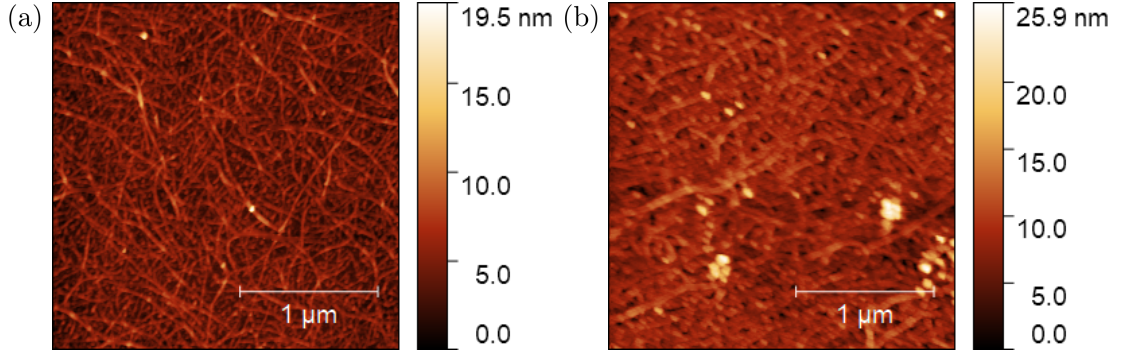


Figure 1.2.: Atomic force microscope images of the channel region of carbon nanotube network devices before and after functionalisation. The channel network of a pristine device is shown in (a), while (b) is of channel 7 from the sensing device functionalised in this section.

Atomic force microscope images of the device channels both before functionalisation and after sensing with the functionalised device to confirm the presence of nanodiscs. As far as the author knows, these are the first atomic force microscope images taken of iOR nanodiscs found on a sensing channel rather than on a separate carbon nanotube film; the wider 20  $\mu\text{m}$  encapsulation mask discussed in [?@sec-encapsulation](#) made this possible. These images are shown in Figure 1.2. Aggregations of nanodiscs are visible in Figure 1.2 (c)–(d). These nanodisc clusters are especially sizable in the lower half of Figure 1.2 (c), where the two largest clusters are  $200 \pm 10$  nm across at their widest point. However, these features are still much smaller than most of the agglomerated nanodisc features seen by Murugathas *et al.* [1]. Furthermore, the nanodisc features closely follow the carbon nanotube bundles across the densely bundled morphology used by Murugathas *et al.* [1]. On the dense network morphology used here, the position of nanodisc clusters relative to the carbon nanotubes is less distinct. To confirm whether nanodiscs have preferentially attached to the carbon nanotubes, a more quantitative approach is needed.

The average height of the substrate was found for both pristine and functionalised atomic force microscope images using the masking tool in Gwyddion. The masks for each image are shown in Figure 1.3. Average substrate heights of  $2.5 \pm 0.2$  nm and  $3.3 \pm 0.4$  nm were found for the pristine and functionalised networks respectively, both within one standard deviation of the substrate height of the steam-assisted surfactant-deposited film analysed in [?@sec-pristine-AFM](#). In Gwyddion, both networks were simplified to a binary representation, where features above a certain threshold were shown as white and features below shown as black, as shown in Figure 1.4. This representation has the appearance of a cross-section through the network at the threshold height. The threshold was chosen as the minimum height where carbon nanotube spindles were no longer apparent in the functionalised image, 8.7 nm above the substrate. Figure 1.4 (a) shows only a few, sparsely distributed features, the majority of which are below 50 nm. These

## 1.2. Aqueous Sensing of Ethyl Hexanoate with OR22a-functionalised Carbon Nanotube Transistor

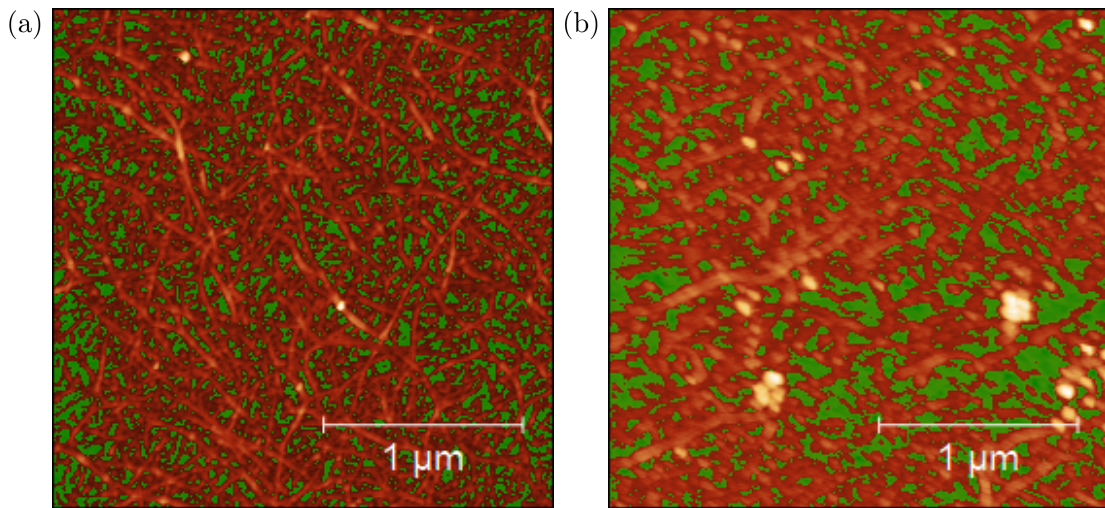


Figure 1.3.: Atomic force microscope images with the substrate background highlighted with a green mask. Here, (a) shows a device channel after functionalisation with PBASE and methanol, while (b) shows channel 7 from the sensing device functionalised with OR22a nanodiscs in this section.

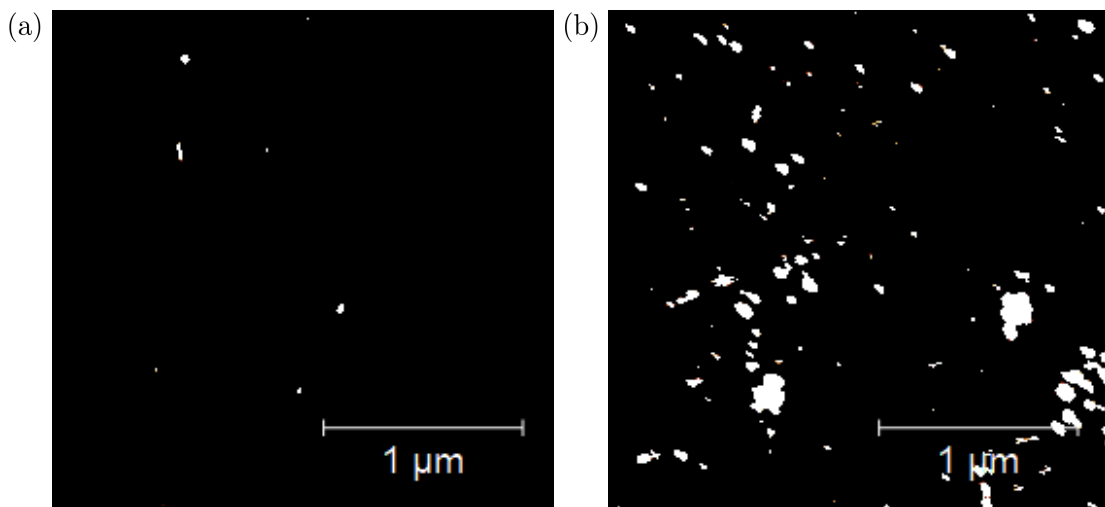


Figure 1.4.: Binary representations of the atomic force microscope images of (a) the pristine device, with a threshold height of 11.2 nm, and (b) the functionalised device, with a threshold height of 12 nm. Both thresholds are 8.7 nm above the substrate background of their respective images.

## 1. Biosensing with Insect Odorant-Receptor Functionalised Carbon Nanotube Devices

features may correspond to surfactant or other surface contamination (**?@sec-pristine-morphology**). In Figure 1.4 (b), many features are over 50 nm across, and often form clusters which sometimes follow curved lines across the network; these patterns give a strong indication that nanodiscs are attaching to the carbon nanotubes.

As the maximum height of the functionalised AFM is 25.9 nm and only nanodisc features are present at 12.0 nm, there must be nanodisc agglomerates present at least 13.9 nm tall. The estimated height range for nanodiscs is  $\sim 10 - 20$  nm [4]–[6]. Assuming a average carbon nanotube height of 1.45 nm, with a average substrate height of 3.3 nm, the nanodisc agglomerations could be up to  $\sim 21$  nm tall. Note that height measurements of biological samples taken via AFM have been shown to underestimate actual feature height by over 50% [7]. Even so, the breadths of the nanodisc features are significantly greater than their heights. While the cross-sections of the largest features are up to 20 nanodiscs across, they are a few nanodiscs high at most; certainly less than five. It appears that, rather than clustering together in solution and attaching as an aggregate, the nanodiscs are individually attaching to preferred locations on the network. These locations may be at junctions between two large carbon nanotubes, which have a relatively large surface area available for binding, or at locations particularly clean of contamination. AFM images showing iOR-nanodisc functionalised carbon nanotube networks with significant vertical clustering have been reported, but these images were not of channels used for sensing [1].

### 1.2.2. Aqueous Sensing of Ethyl Hexanoate

The procedure used for biosensor detection of ethyl hexanoate in liquid was the same as the procedure outlined in **?@sec-dummy-sensing**, except 0.5% DMSO was present in the buffer solution (to improve ethyl hexanoate solubility) and dilutions of ethyl hexanoate in the same 0.5% DMSO 1XPBS buffer solution were added during the sensing series. The 0.5% DMSO 1XPBS was prepared by adding 5  $\mu$ L of DMSO to 995  $\mu$ L 1XPBS before device characterisation. The dilutions of ethyl hexanoate were prepared with the same 1XPBS at the same time, where 5  $\mu$ L of 200 fM, 200 pM, 200 nM and 200  $\mu$ M ethyl hexanoate in DMSO were placed into four individual vials containing 995  $\mu$ L 1XPBS each, giving 1mL vials of 1 fM, 1 pM, 1 nM and 1  $\mu$ M ethyl hexanoate in 0.5% DMSO 1XPBS. The ethyl hexanoate in DMSO dilutions were prepared beforehand as a 1:10 dilution series in DMSO using 200 mM stock solution, where dilutions ranged from 20 mM to 200 fM. Sampling measurements were taken using the B1500A semiconductor device analyser, with the transfer measurement in Figure 1.1 (b) taken directly before sensing. The full control series plus sensing sequence is shown in Figure 1.5. Gate current remained negligible across the entire sensing procedure.

The control series for the sensing series is shown in Figure 1.6 (a). No clear stepwise response is seen to buffer additions or subtractions. The functionalised device shows similar baseline drift behaviour to that of a pristine device, with a period of short-term decay quickly yielding to a more long-lived decay behaviour. A linear fit  $I = c_1 t + c_2$  to

## 1.2. Aqueous Sensing of Ethyl Hexanoate with OR22a-functionalised Carbon Nanotube Transistor

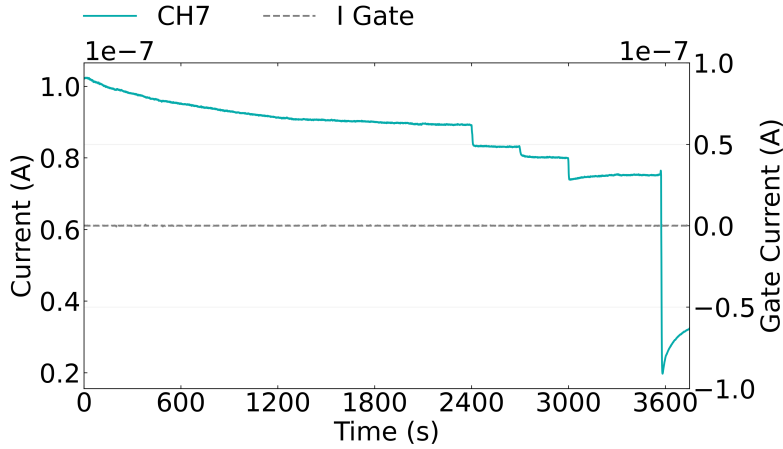


Figure 1.5.: The control series (before 1800 s) and ethyl hexanoate sensing series (after 1800 s) of the OR22a-functionalised device channel. No responses to 0.5% DMSO 1XPBS were seen during the control series, while significant responses to additions of ethyl hexanoate diluted in 0.5% DMSO 1XPBS were seen at 2400 s, 2700 s, 3000 s and 3600 s.

the region  $1200 - 1800$  had a gradient of  $c_1 = -1.76 \pm 0.02$  pA/s. This gradient is smaller than the range of values found for the linear fit approximating the longer-term drift of a pristine device ([?@sec-baseline-drift](#)), but of the same order of magnitude. The linear fit was then subtracted from the control series and an exponential fit  $I = I_0 \exp(-t/\tau)$  was performed on the remaining dataset, as shown in Figure 1.6 (b). A value of  $590 \pm 3$  s was found for the exponential time constant, similar to those found for the channels of the pristine device. This confirms that the 1800 s control series is sufficient to avoid the presence of short-term decay during sensing.

It appears that the exponential fit overestimates current measurements between 1100 s and 1500 s and underestimates between 1500 s and 1800 s. This deviation from the fit may result from the linear approximation used to represent long-term baseline drift being weaker for this channel than for those discussed previously in [?@sec-dummy-sensing](#) and [?@sec-pristine-EtHex](#). This could result from the exponential terms for long-term baseline drift having relatively short time constants, so  $t \ll \tau_i$  no longer holds and higher order terms in the linear approximation are no longer negligible. This observation may indicate a relationship exists between device functionalisation and the long-lived device decay behaviour. However, it may simply result from the natural variation between randomly-deposited device channels. Further work may be required to confirm the existence of such a relationship, though this work is outside the scope of this thesis.

Figure 1.7 (a) shows the cleaned and filtered ethyl hexanoate sensing data from the OR22a-functionalised device from 1800 s onwards. The concentration of each 20  $\mu$ L addition is indicated above the corresponding addition time. The source-drain current

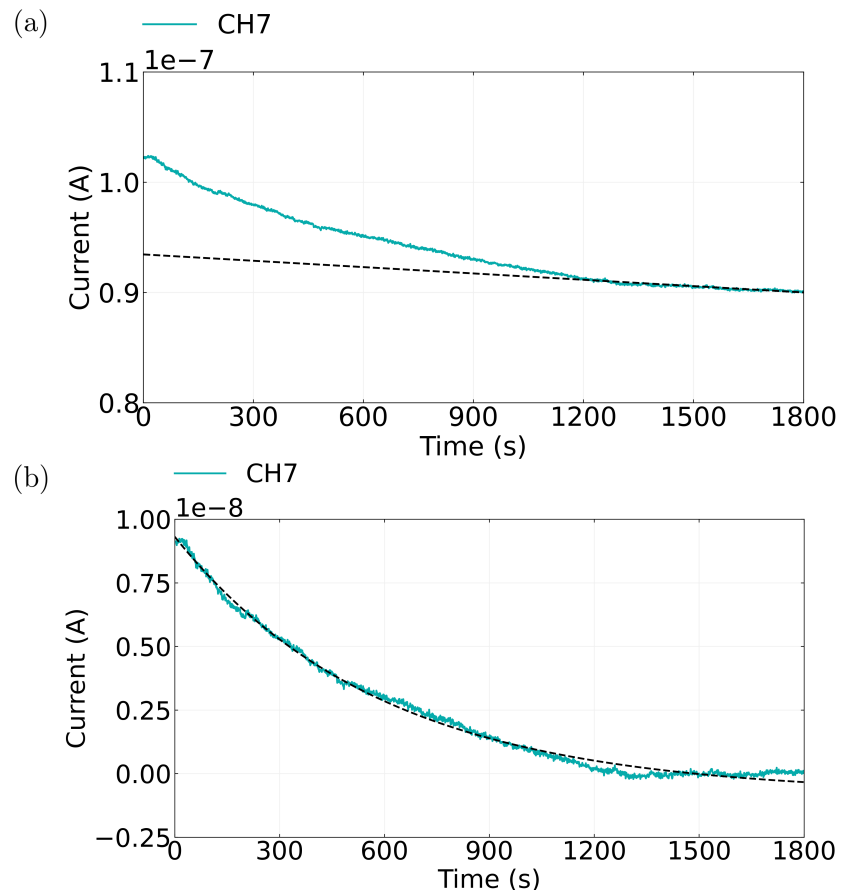


Figure 1.6.: The control series for the OR22a-functionalised device is shown in (a), alongside an extrapolated linear fit to the control series from 1200 s onwards. The control series with the linear approximation subtracted fitted to an exponential curve is shown in (b).

1.2. Aqueous Sensing of Ethyl Hexanoate with OR22a-functionalised Carbon Nanotube Transistor

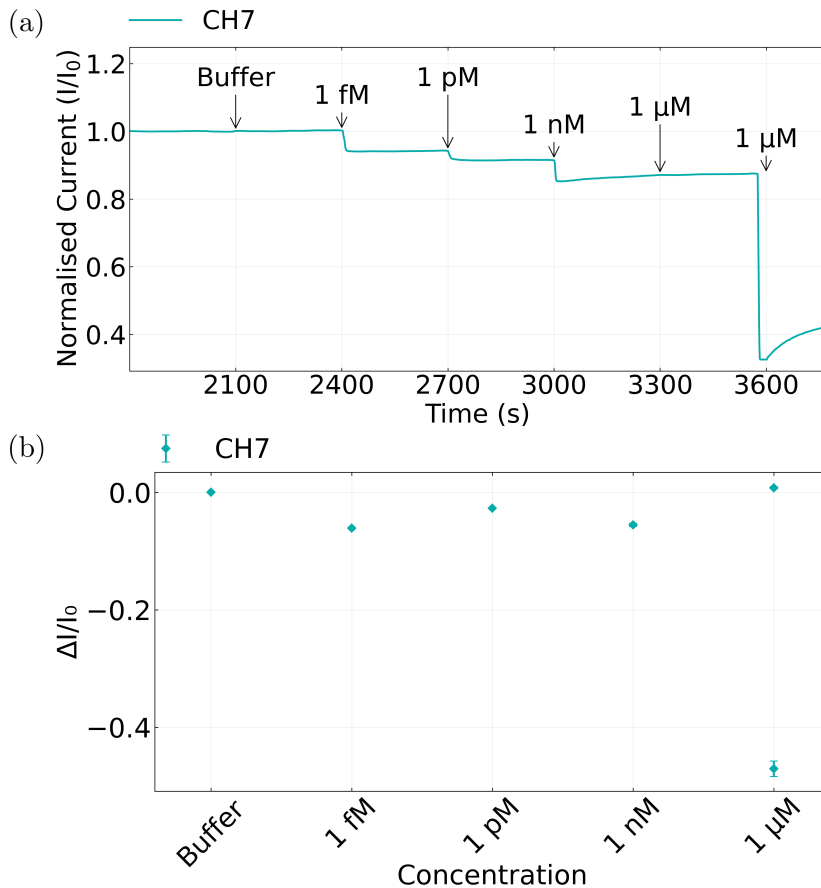


Figure 1.7.: The normalised sensing series for the OR22a-functionalised device is shown in (a). The current data has been despiked, with baseline drift removed and a moving median filter applied. The concentration of each 20  $\mu$ L addition is indicated above the time of addition. The signal data corresponding to the mean difference in current before and after each addition is shown in (b).

## *1. Biosensing with Insect Odorant-Receptor Functionalised Carbon Nanotube Devices*

across the channel decreased rapidly with each addition of ethyl hexanoate in 0.5 DMSO 1XPBS solution. This current decrease appears irreversible, as the current stabilises after each addition at a lower current level than prior to the addition. This behaviour appears to be a response by OR22a to its positive ligand ethyl hexanoate, similar to the response by OR22a to methyl hexanoate seen by Murugathas *et al.*. The presence of the ORCO coreceptor was not required for responses to be seen. The device showed responses to ethyl hexanoate over a wide range of concentrations, beginning with a  $\sim 6\%$  response to 1 fM EtHex in 0.5 DMSO 1XPBS, while showing no response to 0.5% 1XPBS buffer. Interestingly, as seen in Figure 1.7 (b), no clear dose-dependent response was observed. The behaviour seen may be explained by a decreased sensitivity to subsequent additions seen by Murugathas *et al.* [1] competing with the logarithmic increases in the concentration around the channel.

### **1.3. Addressing Biosensor Variability**

#### **1.3.1. Variability in Biosensor Behaviour**

Despite the successful detection of ethyl hexanoate by an OR22a nanodisc-functionalised biosensor in Section 1.2, it was found that this behaviour was not readily reproducible. The results from the previous section were not repeated when using the same procedure for fabrication of devices alongside an identical functionalisation process with the same batch of OR22a nanodiscs (ND-OR22a-SB018). The ethyl hexanoate sensing sequence from six functionalised device channels is shown in Figure 1.8. Figure 1.8 (a) has been left unfiltered to illustrate the variation in behaviour between channels, while Figure 1.8 (b) has been prepared in the same manner as Figure 1.7 (a). The current response to each analyte addition is similar to that seen after the initial addition without ethyl hexanoate present. The largest contributing factor to current change appears to be drift. Unlike the clear decreases in current subsequent to ethyl hexanoate additions seen in Figure 1.7 (a), no decreases are seen in Figure 1.8 (b) to any ethyl hexanoate solution addition.

Liquid-gated electrical characteristics were taken of each sensing channel from this device before and after functionalisation with OR22a, in the same manner as Section 1.2. These characteristics are shown in Figure 1.9. The average threshold shift was  $-0.06 \pm 0.02$ , the same as that of a device functionalised with PBASE in methanol without subsequent functionalisation with OR22a nanodiscs. To test whether protein was present on the channel, an atomic force microscope image was taken of channel 6, as shown in Figure 1.10. The same image analysis as in Section 1.2 was performed, with the substrate mask shown in Figure 1.11 (a) giving an average substrate height of  $3.8 \pm 0.4$ . A binary representation of the image with a 12.5 nm threshold, 8.7 nm above the average substrate height, is shown in Figure 1.11 (b). As with the functionalised device in Figure 1.4 (b), Figure 1.11 (b) shows clustering of features, many of which are larger than 50 nm across. It seems, therefore, that nanodisc aggregates up to 27.5 nm high are present on channel 6, despite the lack of a significant threshold shift as a result of functionalisation.

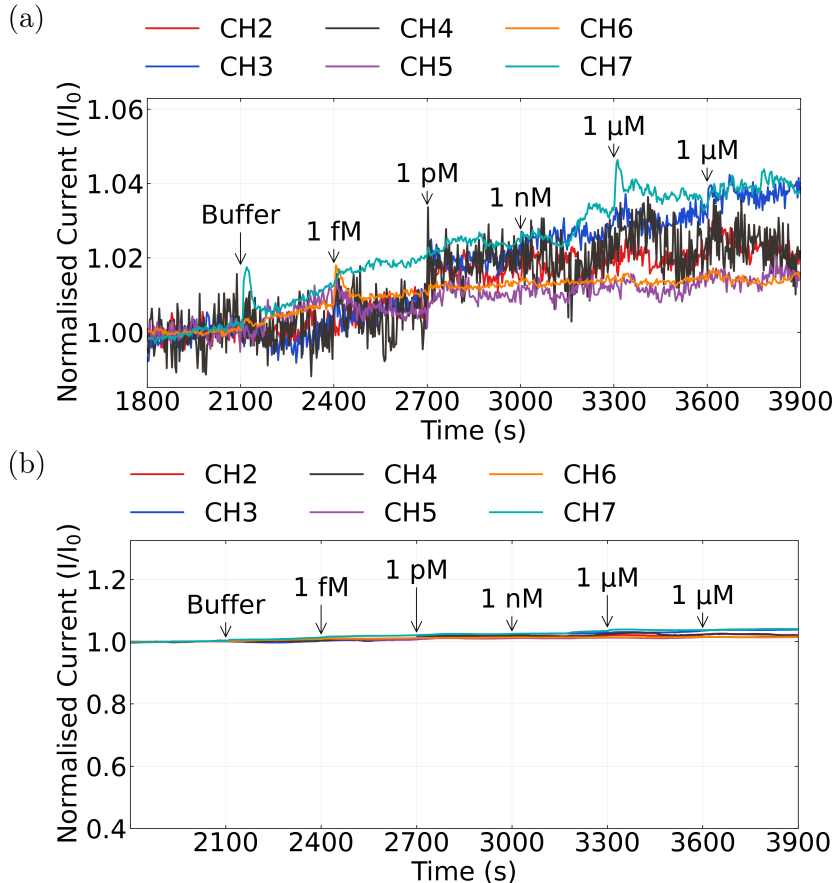


Figure 1.8.: The normalised sensing series of another OR22a-functionalised device across six multiplexed channels, where current data has been despiked and baseline drift removed. The concentration of each  $20 \mu\text{L}$  addition is indicated above the time of addition. The same sensing series is shown in both (a) and (b), where a moving median filter has been applied in (b).

## 1. Biosensing with Insect Odorant-Receptor Functionalised Carbon Nanotube Devices

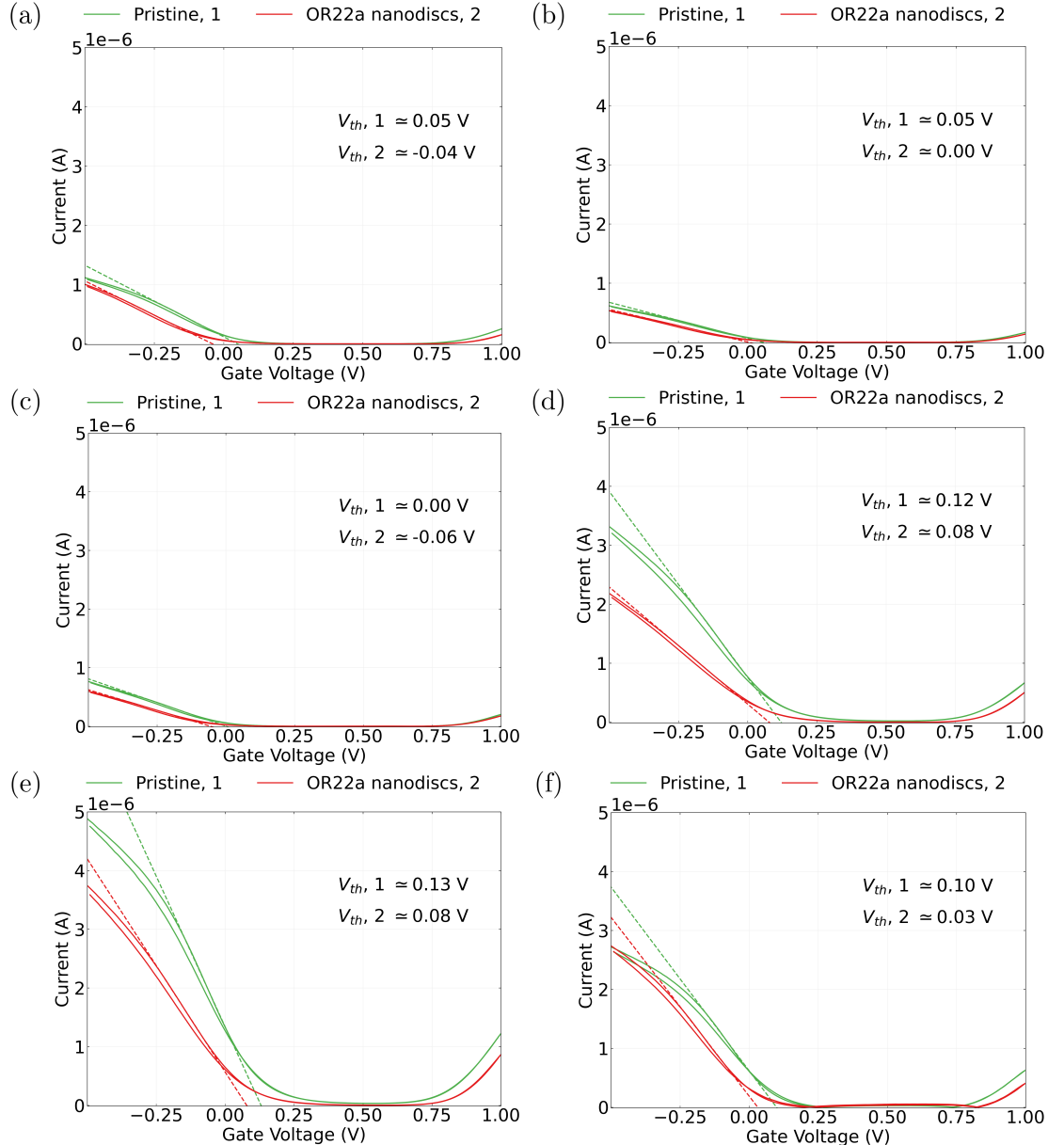


Figure 1.9.: Liquid-gated carbon nanotube network device transfer characteristics before and after OR22a nanodisc functionalisation. Each subfigure (a)-(f) corresponds to a different channel of the functionalised device; (a) corresponds to channel 2, (b) corresponds to channel 3, (c) corresponds to channel 4, (d) corresponds to channel 5, (e) corresponds to channel 6 and (f) corresponds to channel 7. The dashed line shown is tangent to the subthreshold slope of the characteristic curve. The threshold voltage corresponding to the intercept of this slope with the x-axis is shown for each transfer characteristic curve.

### 1.3. Addressing Biosensor Variability

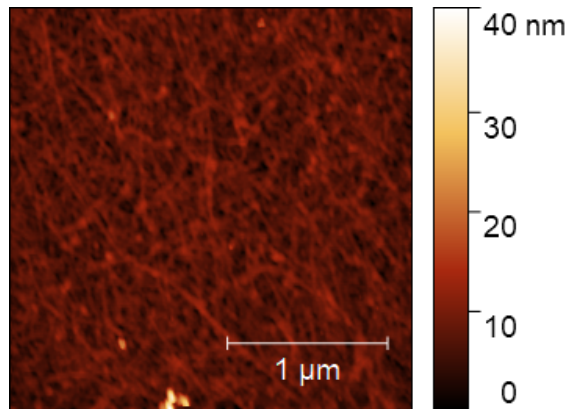


Figure 1.10.: An atomic force microscope image of channel 6 from the OR22a nanodisc functionalised device which showed no response to ethyl hexanoate.

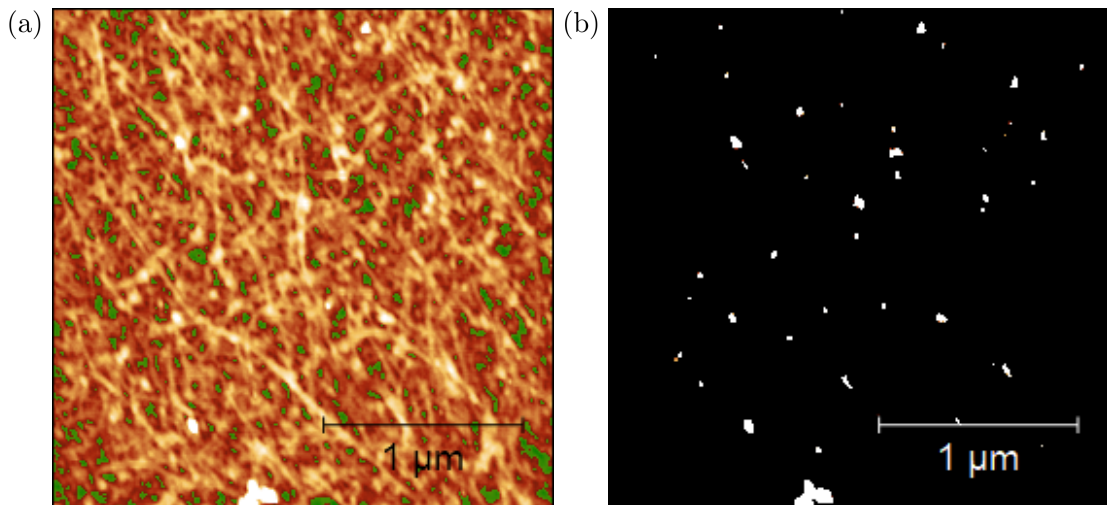


Figure 1.11.: The mask used to find the average substrate height of the functionalised channel 6 is shown in (a), with the substrate highlighted green. The bounds of the colour map have been lowered in (a), as colour mapping over the full height range makes it difficult to clearly distinguish between sub-20 nm features and the substrate. A binary representation of the atomic force microscope image with a threshold height of 12.5 nm is shown in (b).

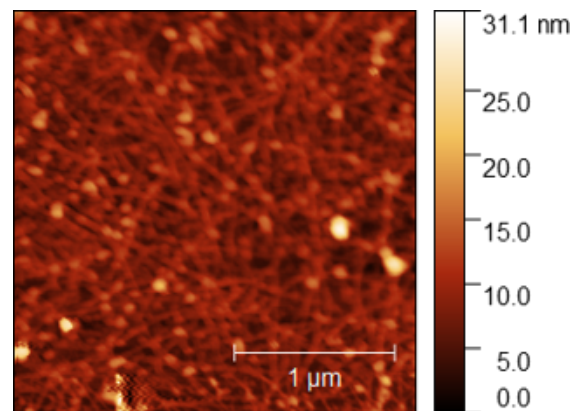


Figure 1.12.: An atomic force microscope image of a carbon nanotube film submerged in OR22a nanodiscs for 1 hour without prior exposure to PBASE or methanol.

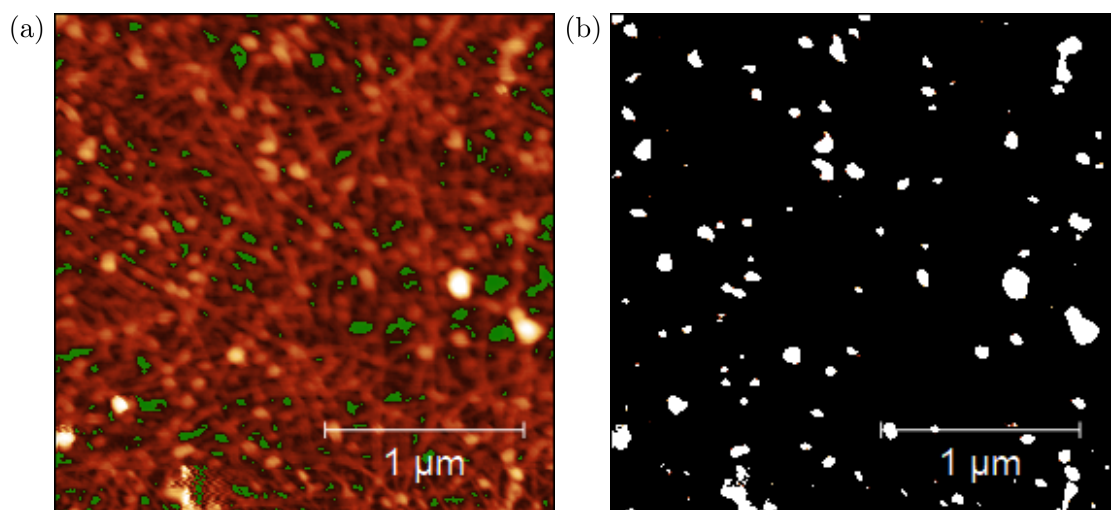


Figure 1.13.: The binary representation of the network, with a height threshold of 12.8 nm (average substrate height = 4.1 nm), is shown in (b).

### 1.3. Addressing Biosensor Variability

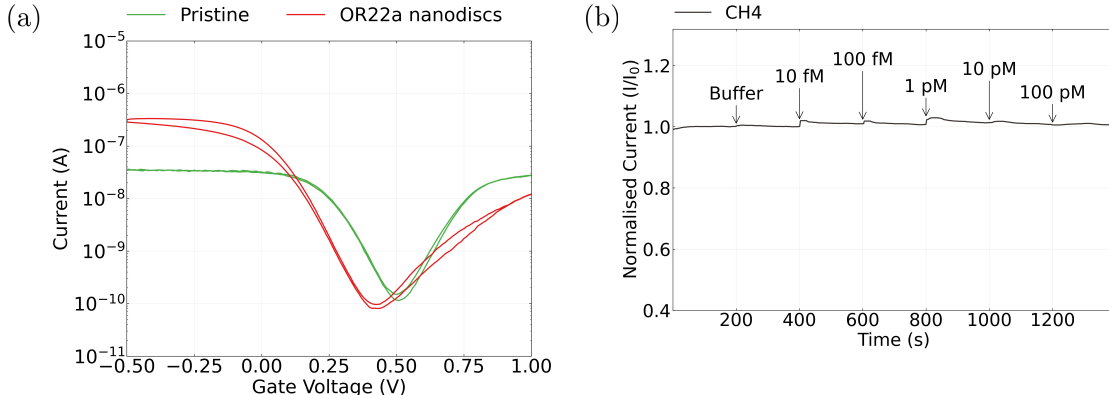


Figure 1.14.: The device characteristics in (a) are from channel 4 of the device placed in OR22a nanodisc solution for 1 hour without prior exposure to PBASE or methanol before and after functionalisation. Real-time sampling using this channel is shown in (b). A 20  $\mu$ L addition of 1% DMSO 1XPBS was made at 200 s. Subsequently, 20  $\mu$ L additions of ethyl hexanoate diluted in 1% DMSO 1XPBS were made at 400 s, 600 s, 800 s and 1000 s and 1200 s, with the concentration of each addition indicated above the time of addition.

Both OR nanodisc and empty nanodisc attachment via PBASE have been shown to cause significant gating of the network (Section 1.2). Therefore, it might be reasoned that the lack of a gating effect, but with nanodiscs present, results from a direct attachment mechanism circumventing the PBASE linker. The amine group on proteins can be attached directly onto carbon nanotubes by adsorption, although this attachment is relatively weak [2]. Figure 1.12 shows an AFM image of a carbon nanotube network film after submersion in a 10 L/mL OR22a nanodisc in PBS solution for 1 hour (batch NDOR22a-0016-1), without prior exposure to PBASE in methanol. Figure 1.13 shows the substrate mask in (a) and a binary representation of this AFM with nanodisc aggregates clearly visible in (b). In Figure 1.14 (a), the negative threshold shift of a channel modified in this way was -0.27 V, similar in size to the shift due to functionalisation seen for the working biosensor. However, this device channel did not work as a sensor when tested with ethyl hexanoate. Figure 1.14 (b) shows a small, positive current response to additions of ethyl hexanoate diluted in 1% DMSO 1XPBS, which may result from the weakly attached OR22a nanodiscs being mechanically removed by the pressure of each addition on the device channels.

An explanation is required for the seemingly contradictory situation where nanodiscs can be present on a device channel without significant gating effects. The most straightforward explanation is that no reliable correlation exists between the two phenomena. Given the consistent threshold shift results for various linker functionalisations seen in **?@sec-noncovalent-functionalisation**, this scenario implies a significant variation in protein structure and charge behaviour within a single nanodisc batch, which seems

## *1. Biosensing with Insect Odorant-Receptor Functionalised Carbon Nanotube Devices*

unlikely. Another possibility is that some type of surface coating is causing nanodiscs to not attach to either PBASE or the carbon nanotubes. This surface coating might be attractive, attaching to both nanodiscs and carbon nanotubes, but forming a barrier layer between the two. Alternatively, this coating might be repulsive, causing nanodiscs to attach weakly to the substrate around the carbon nanotubes. Variations in the degree to which a network is coated may then explain why the same functionalisation method might work for one device but not another. The following section investigates ways of eliminating possible sources of surface coating for more reliable functionalisation results.

### **1.3.2. Potential Sources of Variability**

Throughout the course of this thesis, multiple potential candidates for the unwanted surface coating discussed in the previous section have been identified. These include the surfactant used in carbon nanotube deposition (**?@sec-pristine-morphology**, **?@sec-pristine-electrical-characterisation**) and the solvent used in functionalisation (**?@sec-PBASE-electrical-characterisation**). Another possibility is that PBASE itself is acting as a surface coating, which could result from multilayer coverage restricting access to directly attached PBASE (**?@sec-PBASE-attachment**). Alternatively, PBASE may have hydrolysed into PBA prior to attachment, forming an inert surface layer upon  $\pi$ -stacking around the carbon nanotubes. However, no threshold shift directly attributable to PBA attachment should occur (**?@sec-PBA-characterisation**), and this is not what was observed when characterising the non-working device in Section 1.3. To understand which of these candidates is responsible for the significant variability in biosensor functionality, the sensing procedure was performed with slight variations on the biosensor fabrication and functionalisation procedures. In each test, an individual element of one of these procedures was altered to prevent the introduction of a specific surface coating. The biosensor was then characterised and tested to see if it would respond to its target odorant.

#### **Surfactant Contamination**

Two different approaches were trialled to eliminate possible surfactant contamination, both of which drew heavily on previous methods used for iOR biosensor fabrication [1], [6]. Solvent-deposited carbon nanotube network and graphene devices were fabricated as described in **?@sec-qw-processing**. The same functionalisation process for each device was used as described in Section 1.2.1 with OR22a nanodiscs.

The normalised sensing behaviour for the solvent-deposited carbon nanotube device is shown in Figure 1.15. The device is largely unresponsive at each addition, with a slight current increase on four channels with the 10 fM ethyl hexanoate addition, and a slight decrease on five channels with the 100 fM EtHex addition. No current change exceeded 2%, and as shown in Figure 1.15 (b), the current changes appear negligible on the scale of

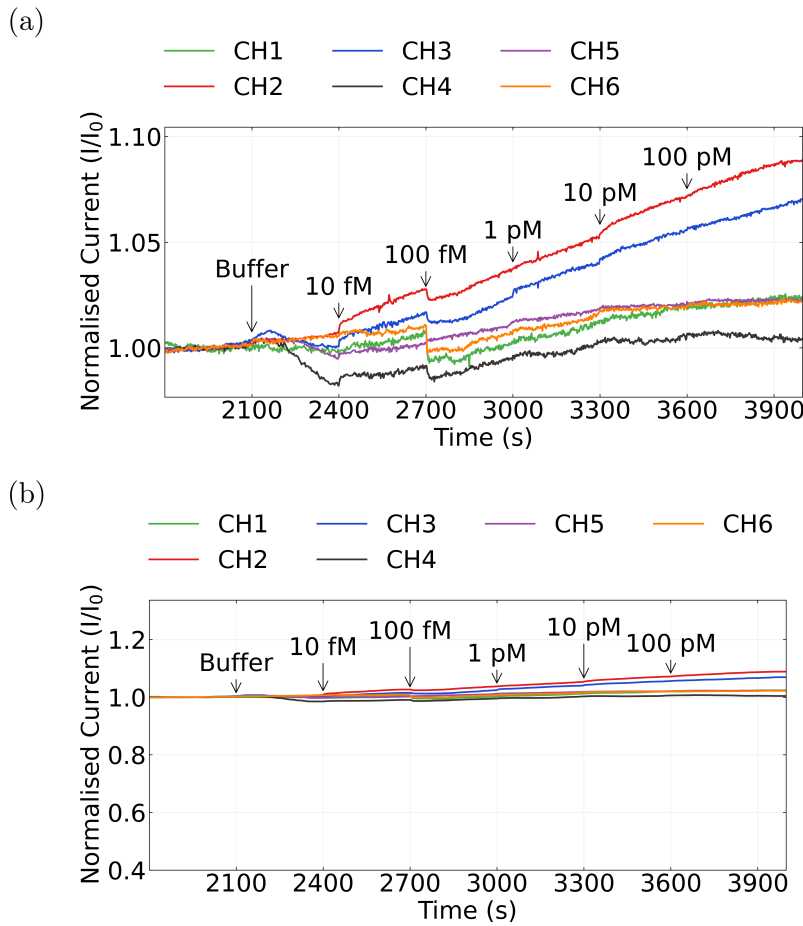


Figure 1.15.: The normalised sensing series of the solvent-deposited, OR22a-functionalised device across six multiplexed channels, where current data has been despiked and baseline drift removed. The concentration of each  $20 \mu\text{L}$  addition is indicated above the time of addition. The same sensing series is shown in both (a) and (b), where a moving median filter has been applied in (b).

## 1. Biosensing with Insect Odorant-Receptor Functionalised Carbon Nanotube Devices

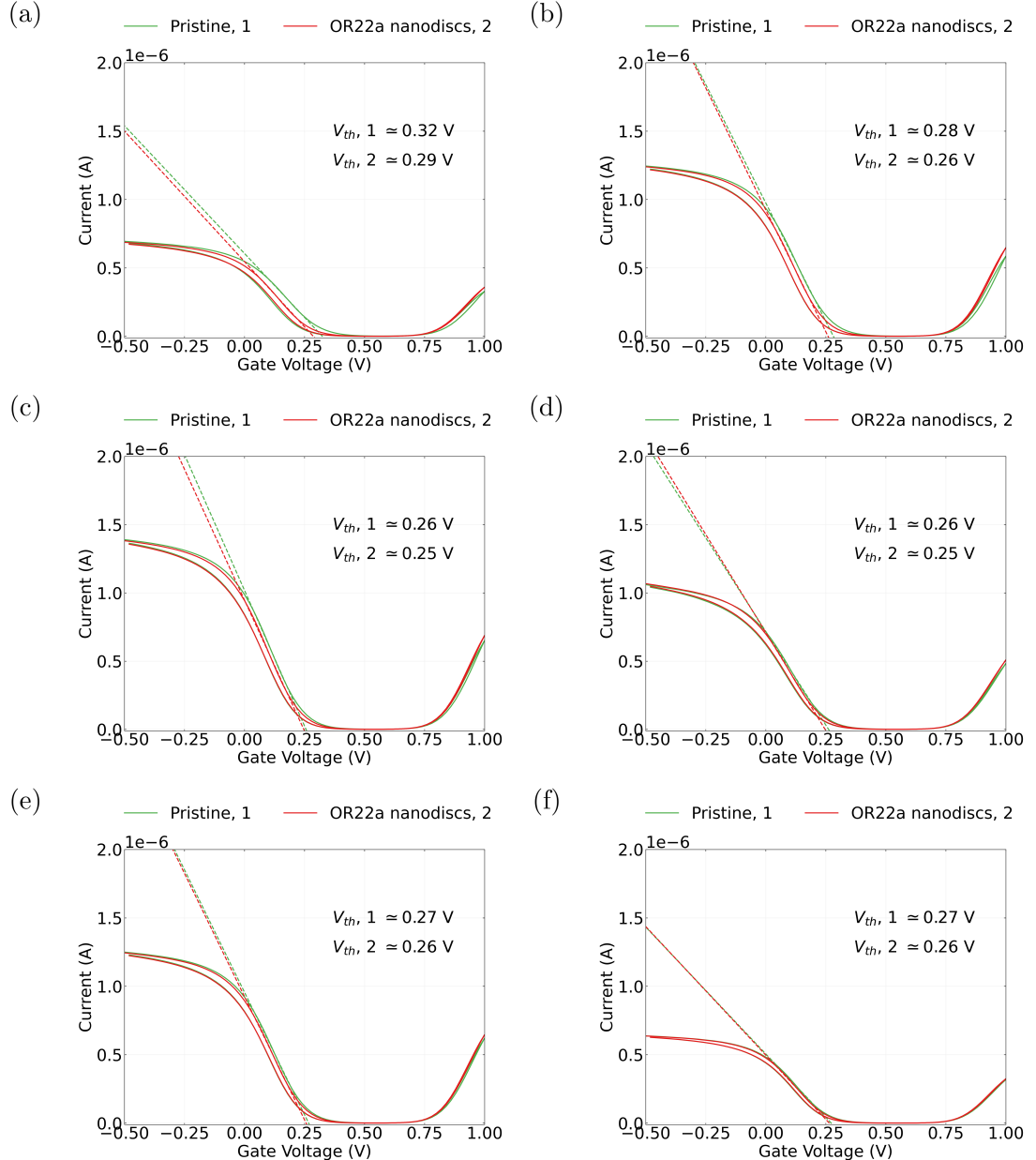


Figure 1.16.: Liquid-gated solvent-deposited carbon nanotube device transfer characteristics before and after OR22a nanodisc functionalisation. (a) corresponds to channel 2, (b) corresponds to channel 3, (c) corresponds to channel 4, (d) corresponds to channel 5, (e) corresponds to channel 6 and (f) corresponds to channel 7. The dashed line shown is tangent to the subthreshold slope of the characteristic curve. The threshold voltage corresponding to the intercept of this slope with the x-axis is shown for each transfer characteristic curve.

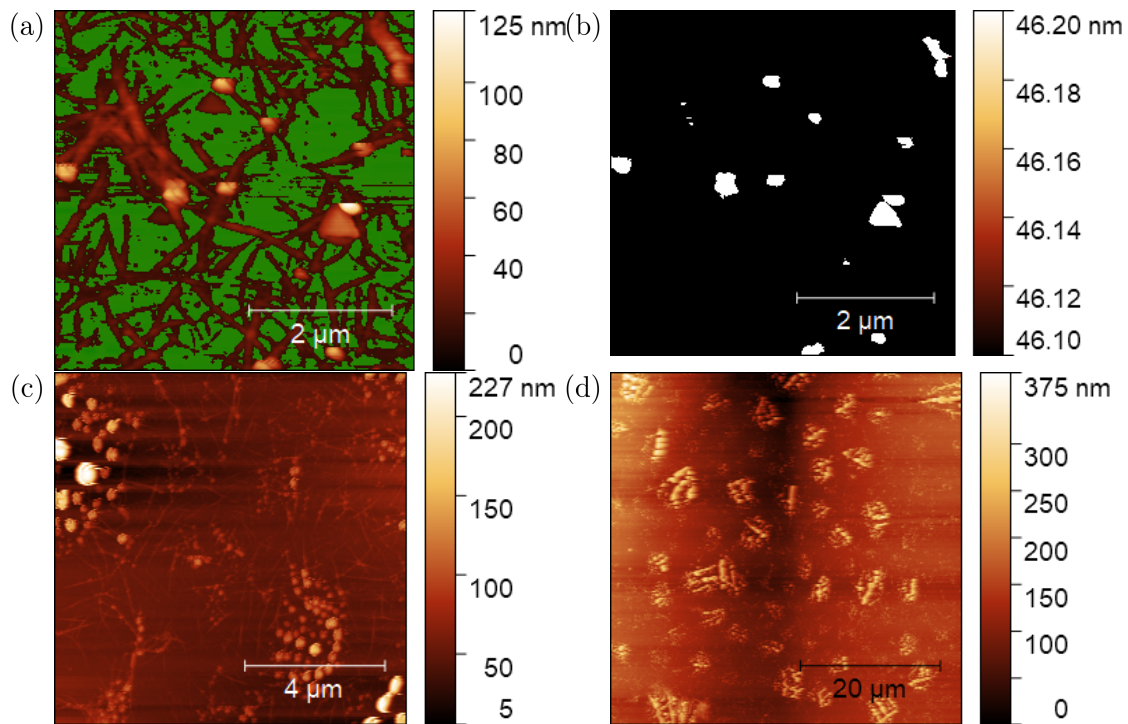


Figure 1.17.: An  $2.5 \mu\text{m} \times 2.5 \mu\text{m}$  atomic force microscope image of an OR22a nanodisc functionalised solvent-deposited carbon nanotube film is shown in (a), with the average substrate height highlighted green. A binary representation of the atomic force microscope image with a threshold height of 34.7 nm is shown in (b).  $10 \mu\text{m} \times 10 \mu\text{m}$  and  $50 \mu\text{m} \times 50 \mu\text{m}$  atomic force microscope images of another film functionalised in the same manner are shown in (c) and (d) respectively.

## 1. Biosensing with Insect Odorant-Receptor Functionalised Carbon Nanotube Devices

the changes seen in Section 1.2.2. The average threshold shift from functionalisation was  $-0.02 \pm 0.01$  V, which indicates attachment of PBASE but not nanodiscs. As the device was made using the pre-2023 encapsulation mask, an AFM was taken of a separate film modified in the same manner, shown in Figure 1.17 (a). The average substrate height was  $11.3 \pm 0.9$  nm. A binary representation of the image taken at the minimum height no spindle-like bundles were visible, 46.1 nm, is shown in Figure 1.17 (b). Attached nanodisc aggregations are clearly visible, and appear closer in nature to those observed for an OR35a-functionalised film [6] than previously seen in this work. Figure 1.17 (c) and (d) show that over a larger scale these aggregations can be at least 330 nm tall, forming large clusters which may indicate mutual interaction during deposition.

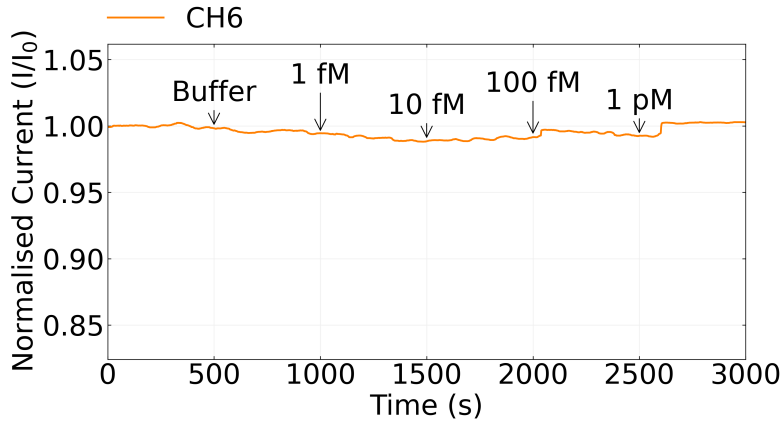


Figure 1.18.: A normalised ethyl hexanoate sensing series taken with a OR22a-functionalised graphene device. The concentration of each 20  $\mu$ L addition is indicated above the time of addition, with additions made at 500 s, 1000 s, 1500 s, 2000 s and 2500 s.

Normalised sensing data from a graphene field-effect transistor functionalised with OR22a nanodiscs in the manner outlined previously is displayed in Figure 1.18. Again, the device shows little response to additions, with no current change resulting from an addition exceeding 1% of the current reading before that addition. This contrasts with the device behaviour observed by Murugathas *et al.*, target analyte additions above 10 fM caused an OR22a nanodisc-functionalised graphene device to exhibit current changes which consistently exceeded 2% [6]. The electrical characteristics of the channel used before and after sensing are shown in Figure 1.19 (a), with a order of magnitude decrease in on-current and negatively shifted Dirac point, similar to the effects of functionalisation observed previously with working OR22a nanodisc GFET biosensors [6]. Intriguingly, Figure 1.19 (b) shows that when modified directly with OR22a nanodiscs without exposure to PBASE and methanol, a larger negative shift in the Dirac point is observed, reflecting the gating behaviour seen for carbon nanotube devices functionalised with and without PBASE in methanol in Section 1.3.1. The similarity between results may imply that the large change in characteristics seen in Figure 1.19 (a) may be primarily due to the effect of methanol and PBASE as in the

### 1.3. Addressing Biosensor Variability

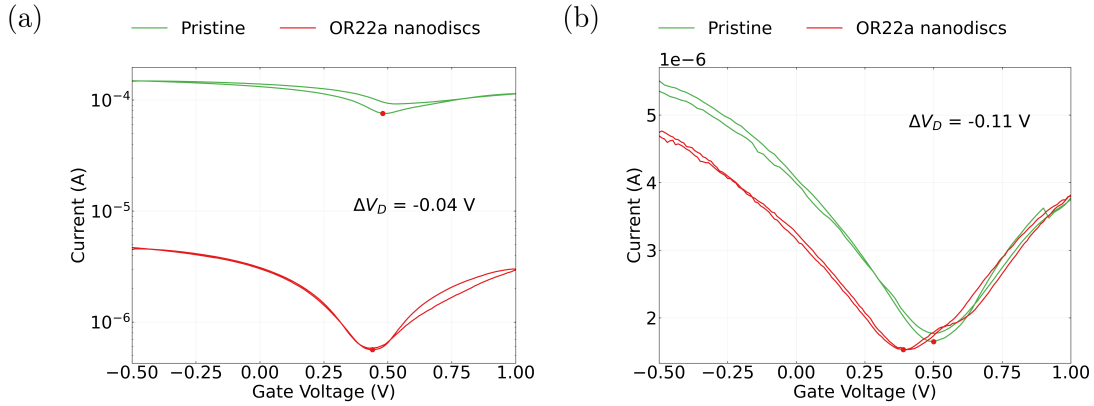


Figure 1.19.: Liquid-gated graphene device transfer characteristics before and after OR22a nanodisc functionalisation. (a) corresponds to a device functionalised, where (a) was functionalised using the standard method while (b) was functionalised without submerging the device in PBASE and methanol. The shift in Dirac point resulting from functionalisation is also shown for each device.

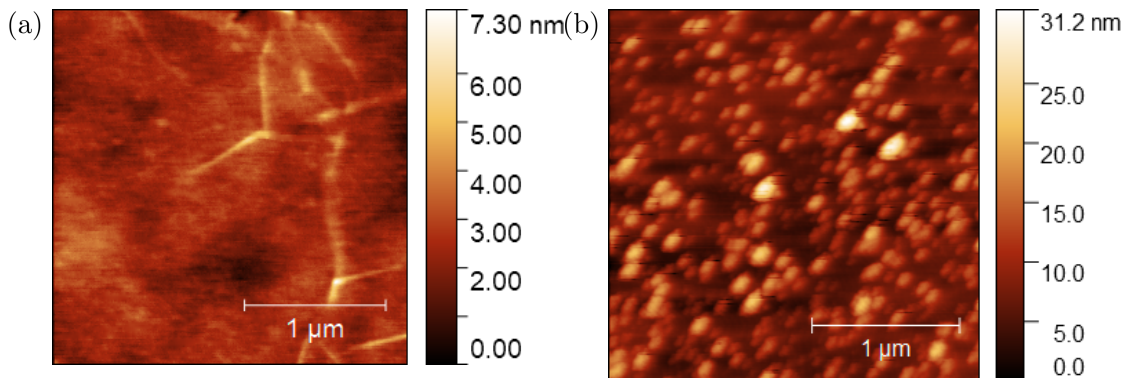


Figure 1.20.:  $2.5 \mu\text{m} \times 2.5 \mu\text{m}$  atomic force microscope images of (a) a monolayer graphene film on  $\text{SiO}_2$  and (b) a graphene film after OR22a nanodisc functionalisation.

## *1. Biosensing with Insect Odorant-Receptor Functionalised Carbon Nanotube Devices*

case of the carbon nanotube network devices.

The surface of a pristine graphene surface and a OR22a-functionalised graphene surface are shown in Figure 1.20 (a) and (b) respectively. Graphene folds of up to 7.3 nm in height are visible on the right hand side of Figure 1.20 (a).

### **PBASE Hydrolysis**

### **Solvent Contamination**

### **1.4. Vapour Sensing**

### **1.5. Conclusion**

## A. Vapour System Hardware

Table A.1.: Major components used in construction of the vapour delivery system described in this thesis.

| Description  | Part No.          | Manufacturer    |
|--|-------------------|-----------------|
| Mass flow controller, 20 sccm full scale           | GE50A013201SBV020 | MKS Instruments |
| Mass flow controller, 200 sccm full scale          | GE50A013202SBV020 | MKS Instruments |
| Mass flow controller, 500 sccm full scale          | FC-2901V          | Tylan           |
| Analogue flowmeter, 240 sccm max. flow             | 116261-30         | Dwyer           |
| Micro diaphragm pump                               | P200-B3C5V-35000  | Xavitech        |
| Analogue flow controller, for micro diaphragm pump | X3000450          | Xavitech        |
| 10 mL Schott bottle                                | 218010802         | Duran           |
| PTFE connection cap system                         | Z742273           | Duran           |
| Baseline VOC-TRAQ flow cell, red                   | 043-951           | Mocon           |
| Humidity and temperature sensor                    | T9602             | Telaire         |
| Enclosure, for humidity and temperature sensor     | MC001189          | Multicomp Pro   |



## B. Python Code for Data Analysis

### B.1. Code Repository

The code used for general analysis of field-effect transistor devices in this thesis was written with Python 3.8.8. Contributors to the code used include Erica Cassie, Erica Happe, Marissa Dierkes and Leo Browning. The code is located on GitHub and the research group OneDrive, and is available on request.

### B.2. Atomic Force Microscope Histogram Analysis

The purpose of this code is to analyse atomic force microscope (AFM) images of carbon nanotube networks in .xyz format taken using an atomic force microscope and processed in Gwyddion (see [?@sec-afm-characterisation](#)). It was originally designed by Erica Happe in Matlab, and adapted by Marissa Dierkes and myself for use in Python. The code imports the .xyz data and sorts it into bins 0.15 nm in size for processing. To perform skew-normal distribution fits, both *scipy.optimize.curve\_fit* and *scipy.stats.skewnorm* modules are used in this code.

### B.3. Raman Spectroscopy Analysis

The purpose of this code is to analyse a series of Raman spectra taken at different points on a single film (see [?@sec-raman-characterisation](#)). Data is imported in a series of tab-delimited text files, with the low wavenumber spectrum ( $100\text{ cm}^{-1} - 650\text{ cm}^{-1}$ ) and high wavenumber spectrum ( $1300\text{ cm}^{-1} - 1650\text{ cm}^{-1}$ ) imported in separate datafiles for each scan location.

### B.4. Field-Effect Transistor Analysis

The purpose of this code is to analyse electrical measurements taken of field-effect transistor (FET) devices. Electrical measurements were either taken from the Keysight 4156C Semiconductor Parameter Analyser, National Instruments NI-PXIe or Keysight B1500A Semiconductor Device Analyser as discussed in [?@sec-electrical-characterisation](#);

### *B. Python Code for Data Analysis*

the code is able to analyse data in .csv format taken from all three measurement setups. The main Python file in the code base consists of three related but independent modules: the first analyses and plots sensing data from the FET devices, the second analyses and plots transfer characteristics from channels across a device, and the third compares individual channel characteristics before and after a modification or after each of several modifications. The code base also features a separate config file and style sheet which govern the behaviour of the main code. The code base was designed collaboratively by myself and Erica Cassie over GitHub using the Sourcetree Git GUI.

# Bibliography

- [1] Thanihaichelvan Murugathas, Han Yue Zheng, Damon Colbert, et al. “Biosensing with Insect Odorant Receptor Nanodiscs and Carbon Nanotube Field-Effect Transistors”. In: *ACS Applied Materials and Interfaces* 11.9 (Mar. 2019), pp. 9530–9538. ISSN: 19448252. DOI: 10.1021/ACSAMI.8B19433. URL: <https://pubs.acs.org/doi/full/10.1021/acsami.8b19433>.
- [2] K. Bradley, M. Briman, A. Star, et al. “Charge Transfer from Adsorbed Proteins”. In: *Nano Letters* 4.2 (Feb. 2004), pp. 253–256. ISSN: 15306984. DOI: 10.1021/NL034985. URL: <https://pubs.acs.org/doi/full/10.1021/nl034985>.
- [3] Iddo Heller, Anne M. Janssens, Jaan Männik, et al. “Identifying the mechanism of biosensing with carbon nanotube transistors”. In: *Nano Letters* 8.2 (Feb. 2008), pp. 591–595. ISSN: 15306984. DOI: 10.1021/NL072996I. URL: <https://pubs.acs.org/doi/full/10.1021/nl072996i>.
- [4] Abhinav Nath, William M. Atkins, and Stephen G. Sligar. “Applications of phospholipid bilayer nanodiscs in the study of membranes and membrane proteins”. In: *Biochemistry* 46.8 (Feb. 2007), pp. 2059–2069. ISSN: 00062960. DOI: 10.1021/BI602371N / ASSET / IMAGES / LARGE / BI602371NF00005.JPEG. URL: <https://pubs.acs.org/doi/full/10.1021/bi602371n>.
- [5] Timothy H. Bayburt and Stephen G. Sligar. “Membrane protein assembly into Nanodiscs”. In: *FEBS letters* 584.9 (May 2010), pp. 1721–1727. ISSN: 1873-3468. DOI: 10.1016/J.FEBSLET.2009.10.024. URL: <https://pubmed.ncbi.nlm.nih.gov/19836392/>.
- [6] Thanihaichelvan Murugathas, Cyril Hamiaux, Damon Colbert, et al. “Evaluating insect odorant receptor display formats for biosensing using graphene field effect transistors”. In: *ACS Applied Electronic Materials* 2.11 (Nov. 2020), pp. 3610–3617. ISSN: 26376113. DOI: 10.1021/ACSAELM.0C00677/ASSET/IMAGES/LARGE/EL0C00677\_0006.JPG. URL: <https://pubs.acs.org/doi/full/10.1021/acsaelm.0c00677>.
- [7] Dusan Vobornik, Maohui Chen, Shan Zou, et al. “Measuring the Diameter of Single-Wall Carbon Nanotubes Using AFM”. In: *Nanomaterials* 13.3 (Feb. 2023), p. 477. ISSN: 20794991. DOI: 10.3390/NANO13030477. URL: <https://www.mdpi.com/2079-4991/13/3/477>.